# 林昭吟
# 著作目錄

期刊論文

1. Y.S. Chen, E.A. Golygin, A.A. Gavrilyuk, J.G. Lin (2018, Apr). Post-treatment effects on the magnetic anisotropy of iron based metallic amorphous ribbons. *Journal of Magnetism and Magne tic Materials*, 461 (2018) 106-110. (Accepted). MOST 106-2811-M-002-092. 本人為通訊作者.
2. Ashish Chhaganlal Gandhi, Jauyn Grace Lin (2018, Feb). Microwave-assisted synthesis and critical analysis for YBa2Cu3O6+δ nanoparticles. *Superconductor Science and Technology*, 31 (2018) 055002 1-8. (Accepted). MOST 105-2112-M-002-010-MY3. 本人為通訊作者.
3. W. C. Lin, C. L. Tsai, K. Ogawa, S. Yamada, Ashish C. Gandhi, and J. G. Lin (2018, Jan). Interfacial magnetic coupling in hetero-structure of Fe/double-perovskite NdBaMn2O6 single crystal. *APPLIED PHYSICS LETTERS*, 112, 162403 (2018). MOST 105-2112-M-002-010-MY3.
4. H. C. Han, Y. S. Chen, M. D. Davydova, P. N. Petrov, P. N. Skirdkov, J. G. Lin, J. C. Wu, J. C. A. Huang, K. A. Zvezdin, and A. K. Zvezdin (2017, Nov). Spin pumping and probe in permalloy dots-topological insulator bilayers. *Appl. Phys. Lett.* , 111, 182411. MOST 105-2112-M-002-010-MY3.
5. M. Y. Song, G. Y. Luo, J. G. Lin*, M. G. Samant, and S. S. P. Parkin (2017, Nov). Infuence of Magnetic Anisotropy on Inverse Spin Hall Voltage. *SPIN*, 7 1750007. MOST 103-2112-M-002-022-MY3. 本人為通訊作者.
6. S. L. CHENG, T. H. CHUANG and J. G. LIN* (2017, Oct). Spin Diffusion Length in Ferromagnet/Superconductor bilayers. *IEEE Trans. Magn*, 53, 9000104. MOST 105-2112-M-002-010-MY3. 本人為通訊作者.
7. Yi-Chien Weng, G. Y. Luo, C.-T. Liang and J. G. Lin* (2017, Oct). Thickness-dependent self-induced spin-pumping in Cobalt thin films. *IEEE Trans. Magn.*, 53, 4100104. MOST 105-2112-M-002-010-MY3. 本人為通訊作者.
8. B. W. Wu, G. Y. Luo, J. G. Lin, and S. Y. Huang* (2017, Aug). Longitudinal spin Seebeck effect in a half-metallic La0.7Sr0.3MnO3 film. *Phys. Rev. B, rapid communication*, 96, 060402(R). MOST 103-2112-M-002-021-MY3.
9. Feng-Jen Chang, Jauyn Grace Lin, and Ssu-Yen Huang,* (2017, Aug). Robust spin current generated by the spin Seebeck effect. *Phys. Rev. Materials*, 1, 031401(R). MOST 103-2112-M-002-021-MY3.

10. G. Y. Luo, J. G. Lin*, Wen-Chung Chiang*and Ching-Ray Chang (2017, Jul). Spin pump and probe in lanthanum strontium manganite/platinum bilayers. *Scientific reports*, 7: 6612. MOST 105-2112-M-002-010-MY3. 本人為通訊作者.
11. Ashish Chhaganlal Gandhi and Jauyn Grace Lin (2017, Apr). Magnetic resonance study of exchange-biased Ni/NiO nanoparticles. *J. Phys.: Condens. Matter*, 29, 215802. MOST 102-2112-M-002-012-MY. 本人為通訊作者.
12. Ashish Chhaganlal Gandhi, Rajasree Das, Fang-Cheng Chou and Jauyn Grace Lin* (2017, Mar). Magnetocrystalline two-fold symmetry in CaFe2O4 single crystal. *J. Phys.: Condens. Matter*, 29, 175802. 本人為通訊作者.
13. J. W. Lin, J. S. Gardner, C.-W. Wang, G. Deng, C. M. Wu, V. K. Peterson, and J. G. Lin* (2017, Mar). Local bonds anomalies and dynamics in bismuth ferrite. *AIP ADVANCES* , 7, 055836 . MOST 105-2112-M-002-010-MY3. 本人為通訊作者.
14. D. Paul Joseph, J.W. Lin, N. Pavan Kumar, W.C.Chen, J.G. Lin* (2016, Nov). Isovalent Bi3+ substitution induced structural and magnetic transitions in LaMnO3. *J. Mag. Mag. Mat.*, 418, 68 - 75. MOST 099-2112-M-9112-002-MY3. 本人為通訊作者.
15. Ashish Chhaganlal Gandhi, Jauyn Grace Lin* (2016, Oct). Exchange bias in finite sized NiO nanoparticles with Ni clusters. *Journal of Magnetism and Magnetic Materials*, 424, 221. MOST 102-2112-M-002-022-MY. 本人為通訊作者.
16. Ye Jin,Mu-Huai Fang, Marek Grinberg, Sebastian Mahlik, Tadeusz Lesniewski, M.G. Brik, Guan-Yu Luo, Jauyn Grace Lin, and Ru-Shi Liu (2016, Apr). Narrow Red Emission Band Fluoride Phosphor KNaSiF6:Mn4+ for Warm White Light-Emitting Diodes. *ACS Applied Materials and Surface*, 8, 11194?11203. (SCI). MOST 104-2119-M-002-027-MY3. MOST 104-2119-M-002- 027-MY3.
17. Ashish Chhaganlal Gandhi, Hui-Yu Cheng, Yu-Ming Chang and Jauyn Grace Lin* (2016, Mar). Size confined magnetic phase in NiO nanoparticles. *Mater. Res. Express*, 3 (2016) 035017. NTU: 104R4000. 本人為通訊作者.
18. Y.S.Chen, J.G.Lin, I.S.Titov, A.B.Granovsky (2016, Feb). Electron spin resonance probed competing states in NiMnInSi Heusler alloy. *Journal of Magnetism and Magnetic Materials*, 407(1), 365–368. MOST 103-2112-M-002-022-MY3. 本人為通訊作者.
19. Y. S. Chen, K. L. Liang, C. C. Chang, J. G. Lin (2015, Nov). Electron Spin Resonance Study on Room-Temperature Ferromagnetic La0.9Sr0.1MnO3 Nanoparticles. *IEEE TRANSACTIONS ON MAGNETICS*, VOL. 51, NO. 11, NOVEMBER 2015. MOST 103-2811-M-002-182. 本人為通訊作者.

20. G. Y. Luo, M. Belmeguenai, Y. Roussigné, C. R. Chang, J. G. Lin*, and S. M. Chérif (2015, Oct). Enhanced magnetic damping in La0.7Sr0.3MnO3 capped by normal metal layer . *AIP Advances* , 5, 097148. 本人為通訊作者.
21. Y. C. Chao, J.G. Lin*, S.H. Chun, K.H. Kim (2015, Oct). Temperature dependent spin structures in Hexaferrite crystal". *J. Magn. Magn. Mat.* , 397, 2301. 本人為通訊作者.
22. Awadhesh Mani, T. Geetha Kumary and J. G. Lin (2015, Aug). Thickness controlled proximity effects in C-type antiferromagnet/superconductor heterostructure. *SCIENTIFIC REPORTS*, 5, 12780-12784.. 本人為通訊作者.
23. A. M. Zhang, S. L. Cheng, J. G. Lin*, and X. S. Wu (2015, May). Strain controlled orbital state and magnetization in insulating LaMnO3+δ films. *J. Applied Physics*, 117, 17B325. 本人為通訊作者.
24. N. Wu, Y. H. Lin, Y. T. Fanchiang, H. Y. Hung, H. Y. Lin, P. H. Lin, J. G. Lin, S. F. Lee, M. Hong, and J. Kwo (2015, May). Strongly enhanced spin current in topological insulator/ferromagnetic metal heterostructures by spin pumping. *Journal of Applied Physics* , 117, 17D148.
25. S. L. Cheng, J. G. Lin, and T. H. Chuang (2015, Mar). Spin injection induced phase transition in YBa2Cu3O7−δ/Nd0.35Sr0.65MnO3 bilayer. *JOURNAL OF APPLIED PHYSICS*, 117, 17E312. MOST 103-2112-M-002-022-MY3. 本人為通訊作者.
26. W. Q. Liu, M. Y. Song, N. J. Maltby, S. P. Li, J. G. Lin, M. G. Samant, S. S. P. Parkin, P. Bencok, Paul Steadman, Alexey Dobrynin, Y. B. Xu, R. Zhang (2015, Mar). XMCD Study of Epitaxial Magnetite Ultrathin Film on MgO(100) . *Journal of Applied Physics*, 117,17.
27. Ai Mei Zhang and Jauyn Grace Lin (2014, Nov). Competition of spin states in heterogenous LaMnO3+δ. *Japanese Journal of Applied Physics*, 53, 123002. MOST 101-2811-M-002-058. 本人為通訊作者.
28. H. Y. Hung, T. H. Chiang, B. Z. Syu, Y. T. Fanchiang, J. G. Lin, S. F. Lee, M. Hong, and J. Kwo (2014, Oct). Observation of strongly enhanced inverse spin Hall voltage in Fe3Si/GaAs structures. *APPLIED PHYSICS LETTERS*, 105, 152413. MOST 102-2112-M-002-022-MY3.
29. H. Y. Guo, J. G. Lin, Jan Chi Yang, and Y. H. Chu (2014, Sep). Dynamic magnetic interaction in La2/3Sr1/3MnO3/BiFeO3 heterostructure. *APPLIED PHYSICS LETTERS*, 105, 112406. MOST 101-2119-M-009-003-MY2. 本人為通訊作者.
30. Y. S. Chen, Chih-Wei Cheng, G. Chern, and J. G. Lin (2014, Sep). Critical analysis on nanostructured CoFeB synthetic orthogonal ferrimagnet. *JOURNAL OF APPLIED PHYSICS*, 116 , 113904. MOST 102-2112-M-002-012-MY3. 本人

為通訊作者.

31. H. L. Liu, Y. C. Su, Y. H. Tang, and J. G. Lin (2014, Apr). Variation of the lattice and spin dynamics in Bi1 x Dy x FeO3 nanoparticles. *J. Appl. Phys*, 115, 133506. MOST 102-2112-M-003-002-MY3.
32. C.-P. Chang, M.-W. Chu, H.T. Jeng, S.-L. Cheng, J.G. Lin, J.-R. Yang & C.H. Chen (2014, Mar). Condensation of two-dimensional oxide-interfacial charges into one-dimensional electron chains by the misfit-dislocation strain field. *NATURE COMMUNICATIONS*, 10.1038.
33. G. Y. Luo, C. R. Chang, and J. G. Lin (2014, Jan). Influence of damping constant on inverse spin hall voltage of La 0.7 Sr 0.3 MnO 3 (x)/platinum bilayers. *JOURNAL OF APPLIED PHYSICS*, 115, 17C508. MOST 99-2112-M-002-027-MY3. 本人為通訊作者.
34. Wen-Chung Chiang ; Wen-Lin Lan ; Yung-Hsiu Tang ; Lin, J.G. (2014, Jan). Electron Spin Resonance Probed Magnetic Interactions in Fe-, Cr-, and Ni-Doped TiO2. *IEEE TRANSACTIONS ON MAGNETICS*, VOL. 50, NO. 1. MOST 99-2112-M-034-001.
35. C. W. Chong, M. J. Huang, H. C. Han, Y. K. Lin, J. M. Chiu, Y. F. Huang, H. J. Lin, T. W. Pi, J. G. Lin, L. C. Chen, K. H. Chen, and Y. F. Chen (2013, Nov). Resistance memory device of La0.7Sr0.3MnO3 on Si nanotips template. *Applied Physics Letters*, 103, 211606 . 本人為通訊作者.
36. D. Paul Joseph, Daniel Hsu, and J. G. Lin (2013, Jul). Stray field enhanced vortex dissipation in YBa2Cu3O7/La0.7Sr0.3MnO3/YBa2Cu3O7 hetero-epitaxial tri-layer. *Applied Physics Letters*, 103, 012601-012604. 本人為通訊作者.
37. G. Y. Luo , C. R. Chang , and J. G. Lin (2013, Jul). Thickness Dependent Spin Pumping Effects in La Sr MnO /Platinum Bilayer Film. *IEEE TRANSACTIONS ON MAGNETICS*, 49, NO. 7, JULY . 本人為通訊作者.
38. J. G. Lin , M.Y. Song , J.W. Lin , Mahesh G. Samant and Stuart S. P. Parkin (2013, Jul). Ferromagnetic Resonance Study of Fe O Thin Film . *IEEE TRANSACTIONS ON MAGNETICS*, 49, NO. 7, JULY . 本人為第一作者、通訊作者.
39. Daniel Hsu1, Yu-Han Tsai, Zhongwen Xing and Jauyn Grace Lin (2013, Jun). Interface-engineered resistive switching in Ag/SrTiO3/Nd0.7Ca0.3MnO3/YBa2Cu3O7 heterostructures. *THE EUROPEAN PHYSICAL JOURNAL B*, 86, 242-245. 本人為通訊作者.
40. D Paul Joseph and J G Lin (2013, May). Proximity effect in La0.7Sr0.3MnO3-Bi2Sr2CaCu2O8 hybrid bi-layers. *SUPERCONDUCTOR SCIENCE AND TECHNOLOGY*, 26 (2013) 075004 (6pp). 本人為通訊作者.

41. Paul Joseph Daniel and Jauyn Grace Lin (2013, May). Investigation of Optimal Growth Conditions of La0.7Sr0.3MnO3–Bi2Sr2Ca1Cu2O8 Heterostructures. *The American Ceramic Society*, 96 [2] 481–484. 本人為通訊作者.
42. H. Y. Hung, G. Y. Luo, Y. C. Chiu, P. Chang, W. C. Lee, J. G. Lin, S. F. Lee, M. Hong and J. Kwo (2013, Apr). Detection of inverse spin Hall effect in epitaxial ferromagnetic Fe3Si films with normal metals Au and Pt . *JOURNAL OF APPLIED PHYSICS* , 113, 17C507 .
43. T. C. Han and J. G. Lin (2013, Apr). Exchange bias between multiferroic HoMnO3 and ferromagnetic SrRuO3 films . *J. Appl. Phys.* , 113, 17D718.
44. T. C. Han, C. T. Chen, S. S. Pan, and J. G. Lin (2013, Mar). Heterojunction of multiferroic HoMnO3 on Nb-doped SrTiO3 . *J. Appl. Phys.* , 113, 17C709.
45. C.-P. Chang, J. G. Lin, H. T. Jeng, S.-L. Cheng, W. F. Pong, Y. C. Shao, Y. Y. Chin, H.-J. Lin, C. W. Chen,J.-R. Yang, C. H. Chen, and M.-W. Chu (2013, Feb). Atomic-scale observation of a graded polar discontinuity and a localized two-dimensional electron density at an insulating oxide interface. *PHYSICAL REVIEW B* , 87, 075129.

研討會論文

1. D. Paul Joseph, J. G. Lin (2015, Jun). NON-LOCAL SPIN INJECTION EFFECTS IN COPLANAR La0.7Sr0.3MnO3/Bi2Sr2CaCu2O8/La0.7Sr0.3MnO3 TRI-LAYER. AIP, Conference proceeding, Tamilnadu, India . NSC 99-2112-M-002-027-MY3. 本人為通訊作者.

Journal of Magnetism and Magnetic Materials 461 (2018) 106–110

Contents lists available at ScienceDirect

Journal of Magnetism and Magnetic Materials

journal homepage: www.elsevier.com/locate/jmmm

Research articles

# Post-treatment effects on the magnetic anisotropy of iron based metallic amorphous ribbons

Y.S. Chen [a], E.A. Golygin [b], A.A. Gavrilyuk [b], J.G. Lin [a,*]

[a] Center for Condensed Matter Sciences, National Taiwan University, Taipei 10617, Taiwan
[b] Department of Physics, Irkutsk State University, Irkutsk, Russia

ARTICLE INFO

*Article history:*
Received 10 January 2018
Received in revised form 17 April 2018
Accepted 25 April 2018
Available online 26 April 2018

ABSTRACT

The effects of acid and heat treatment on the magnetic anisotropy of amorphous $Fe_{67}Co_{10}Cr_3Si_5B_{15}$ ribbons are studied, using the angular-dependent magnetization and ferromagnetic resonance (FMR). The change of FMR spectrum after acid treatment indicates that the surface precipitates in raw sample contain some magnetic elements. A post annealing under the field of 2000 Oe is applied to modify the magnetic anisotropy of ribbons, with the annealing temperature varying from 370 to 410 °C. At 370 °C, a magnetoelastic anisotropy field of +40 Oe is found in the sample with 60 min acid-treatment, while it is −74 Oe for the sample with 30 min acid-treatment. However, it approaches to zero at 410 °C for all samples, indicating the internal stress is fully released. This study demonstrates that FMR is an effective technique on investigating the details of magnetic anisotropy configuration against various post-treatment conditions for amorphous ribbons.



## 1. Introduction

The amorphous Iron-based alloys are promising materials due to their unique properties [1,2], including high mechanical strength [3], high permeability [4] and low magnetic loss. These properties have advantages for the applications of transformers [1,2], sensors [4] and high performance structures. The amorphous ribbons were often prepared with the spin melting process with fast cooling to form the amorphous structures, and their properties can be further improved with post treatments. Various post treatments such as heat [5–7], plastic deformation [8] and surface treatments [9,10] were applied on raw samples to modify their properties. Among many, the major mechanisms to improve the magnetic properties are identified as 1) the relaxation of internal stresses at elevated temperature, 2) the inducing of anisotropy by magnetic field or/and mechanical stresses and 3) the destabilization of domain walls. However, these mechanisms are sometimes competing with each other and create un-predictable properties. Thus, the correlation between the process conditions and the magnetic property is important, yet to be established due to the very complex configuration of magnetic anisotropy in bulk and surface layer. In such case, an effective and non-destructive method is highly desirable to identify the effect of post treatments.

The field dependent spectrum of ferromagnetic resonance (FMR) is very sensitive to the grain boundary, the grain-grain interaction and the magnetic anisotropy of magnetic materials. The previous FMR work on determining the magnetic anisotropy [11] and the annealing induced crystallization [12] in amorphous ribbons have proved that this non-contact and non-destructive probe could be potentially applicable for a continuous process such as an on-line characterization of materials. In this work, both the FMR and the conventional VSM magnetometer are used to investigate the effects of acid and annealing treatment on the magnetic anisotropy of amorphous $Fe_{67}Co_{10}Cr_3Si_5B_{15}$ alloy ribbons. The field-swept FMR is used to identify the individual component in a system with complex configuration of magnetic anisotropy, which is not possible to achieve by using the traditional DC-magnetization-based technique.

## 2. Experiments

Amorphous $Fe_{67}Co_{10}Cr_3Si_5B_{15}$ ribbons are prepared with typical melting spin method. For FMR measurement, the ribbons are cut into 10 pieces with 30 mm long for each. The size of each sample is around 30 × 0.8 mm with ribbon axis as the long side and a thickness of ~40 μm. The nine raw samples are then divided into three groups and treated with the acid of 0.20 N (Equivalent concentration) HCl for 30, 40 and 60 min, denoted as N3, N4 and N6 series respectively. Following, the three samples in each series are annealed in vacuum at different annealing temperature ($T_A$)

* Corresponding author.
*E-mail address:* jglin@ntu.edu.tw (J.G. Lin).

https://doi.org/10.1016/j.jmmm.2018.04.057
0304-8853/

of 370, 390 and 410 °C for 30 min. The aim of heat-treatment is to remove internal hardening stresses and to induce uniaxial magnetic anisotropy. Therefore, the annealing temperature must be below the temperature of crystallization, yet high enough to release the inner hardening stresses. The reported temperature for the crystallization of FeCoSiB alloy is in the range of 400–500 °C [13]. An in-plane magnetic field of 2000 Oe is applied during the annealing, in the direction transversal to the axis of ribbon. The morphologies of samples are investigated with Scanning Electron Microscopy (SEM; JEOL 6700). The surface chemical composition is determined with Electron Spectroscopy for chemical analysis system (ESCA; VG Scientific ESCALAB 250). FMR measurement is conducted in the $TE_{102}$ cavity of Bruker EMX system at X-band (9.8 GHz) with the applied field along the ribbon axis. Magnetic remanence (R) and hysteresis (M-H) loop are measured with Vibrating Sample Magnetometer (VSM; Microsense EZ) and SQUID magnetometer (Quantum Design MPMS) respectively. The in-plane angular dependent remanence is obtained for N6 series using a square shape of sample to suppress the effect of in-plane shape anisotropy. Samples for the magnetization measurements are cut into the squares with a dimension of 0.8 × 0.8 mm and with the ribbon axis marked in one direction.

## 3. FMR data analysis

FMR spectra could reveal the anisotropy of magnetization based on the value of resonance field ($H_r$) which is defined as the center field of an absorption spectrum. For a thin plate, the out-of-plane anisotropy is dominated by the shape anisotropy, while the in-plane resonance field along the principal axis is given by

$$\omega/\gamma = \sqrt{(H_r + H_\sigma)(H_r + N_d M_s)} \quad (1)$$

where ω and γ are angular frequency and gyromagnetic ratio, respectively. $N_d$ is the demagnetization factor expressing the shape anisotropy and $M_s$ the saturation magnetization. In this study, $N_d$ is a constant for all samples because of a consistent ribbon form for all samples. $H_\sigma$ is the magnetoelastic anisotropy field induced during the heat treatment. In this study, a positive $H_\sigma$ marks a magnetic anisotropy along the ribbon long axis. The crystal anisotropy is negligible in amorphous ribbons. Therefore, the change of $H_r$ is correlated to the variation of $H_\sigma$ in an opposite trend, under the assumption that $M_s$ is kept as a constant within a narrow annealing temperature.

## 4. Result and discussion

Fig. 1(a)–(d) are the SEM images for the three samples with different time of acid etching. Fig. 1(a) is for the as-prepared (raw) sample, showing a high amount of precipitate grains on the surface. Based on our XRD analysis, there is no crystallization in bulk ribbon. The precipitate grains on the surface could be crystalline but was not detected by XRD due to the low intensity. Fig. 1(b) is a magnified view of precipitates. Fig. 1(c) and (d) are the image for the samples with 30 min (N3) and 60 min (N6) respectively. The flat surfaces in (c) and (d) suggest that the precipitates are removed by HCl. Fig. 2 plots the result of ESCA for the Co/Fe ratio against the acid etching time. It shows the Co/Fe ratio increases with etching time, revealing that the partial Fe element is removed from the surface by acid treatment. Inset of Fig. 2 is a typical spectrum of XPS (squares) for Fe element, fitted with a Gaussian curve (solid line).

The M-H loops of raw sample, N3 and N6 are shown in Fig. 3 as open squares, circles and triangles respectively. The difference between each sample is not significant, suggesting that the saturation magnetization is not sensitive to the acid induced surface modification. Inset of Fig. 3 displays the low field region, showing a very low coercivity.

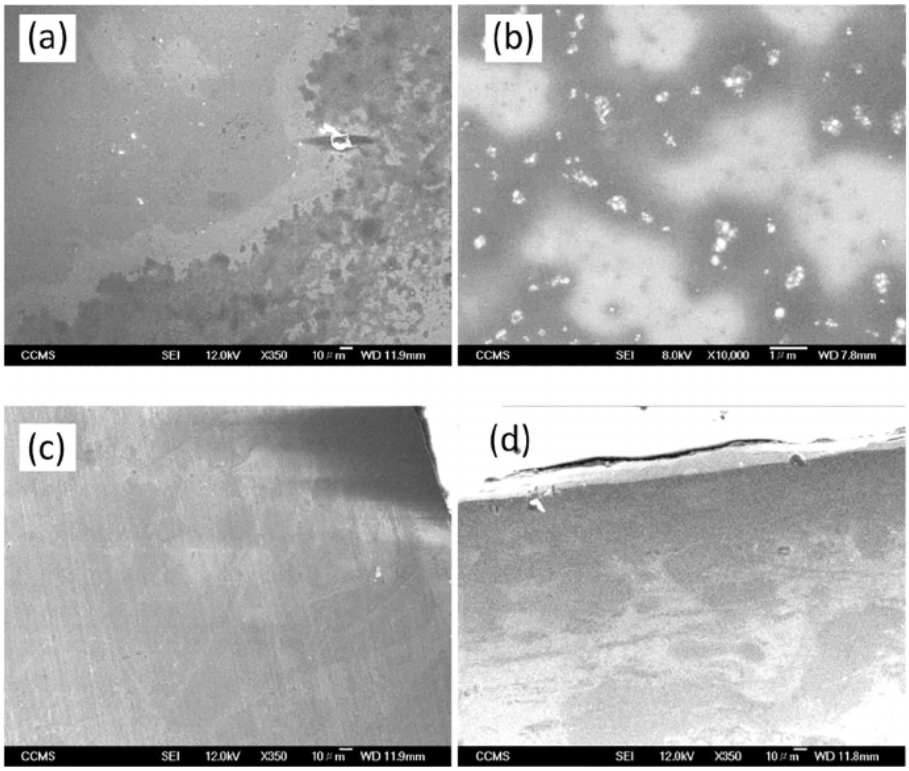


**Fig. 1.** The SEM image for (a) as-prepared raw ribbon, (b) the Magnification of the "rough" region in (a), (c) N3 and (d) N6.

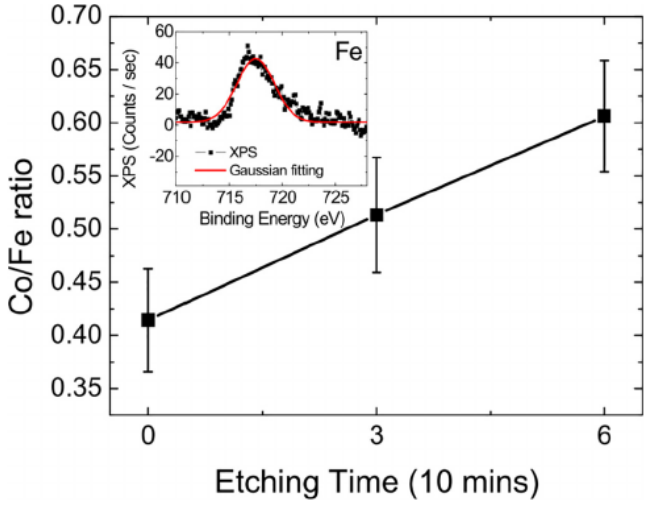


**Fig. 2.** Co/Fe atomic ratio on the surface with carious acid treatment time with lines for eye-guiding. Inset is a typical XPS spectrum of the ribbons near Fe 2p edge with a Lorentz fitting (sold line).

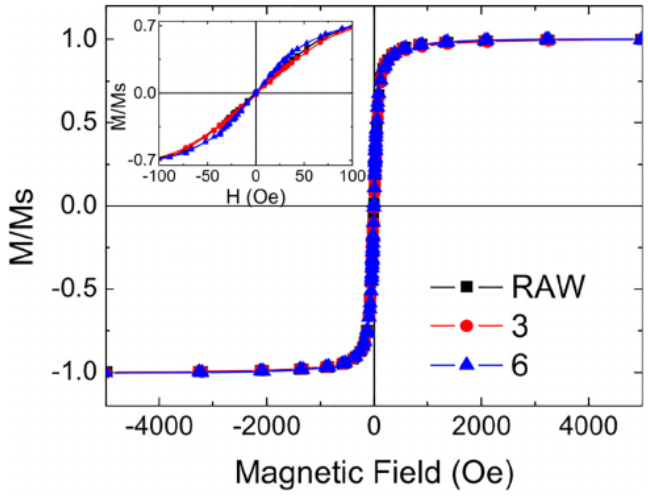


**Fig. 3.** Hysteresis loop for RAW (squares), N3 (circles), and N6 (triangles) samples. Inset is a magnification of low field range.

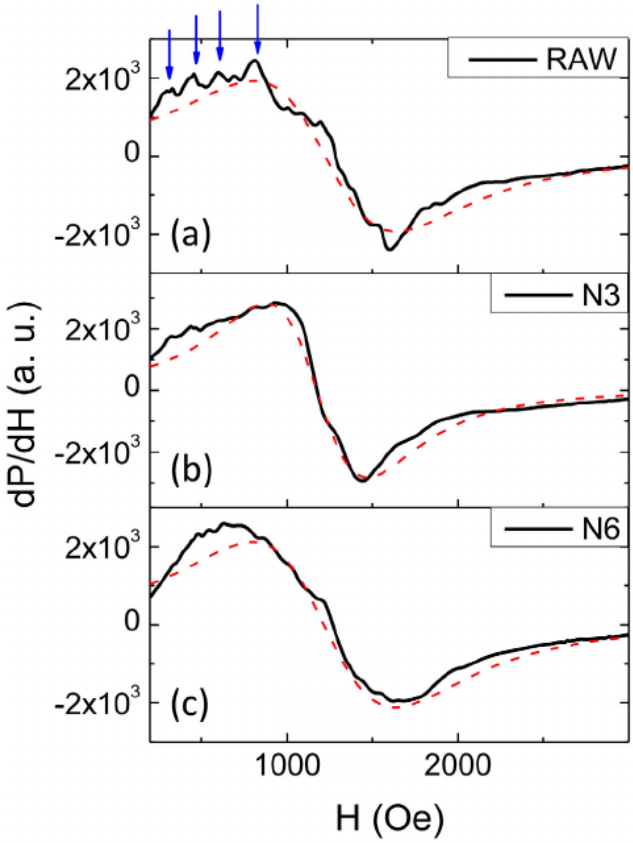


**Fig. 4.** FMR spectra for samples before and after acid treatment. Dash line is the Lorentz fitting for each spectrum showing the ideally symmetric lineshape. Arrows indicate the sharp peaks observed in RAW sample.

Fig. 4 plots the derivative FMR spectra of three samples under different etching time of acid treatment, as shown with the solid lines. All samples display broad Lorentz-like shapes. Dash lines in Fig. 4 are the best fit of Lorentz curves, resembling the ideal absorption spectra. In the low-field region, several small but sharp peaks are observed in the raw sample as indicated by the arrows, suggesting some non-percolated nano-grains [14]. These minor peaks are suppressed after acid treatment, indicating the precipitate grains are removed from the surface. This result demonstrates the sensitivity of FMR spectroscopy to the surface magnetic property is higher than that of M-H measurement.

Fig. 5 shows the FMR spectra for nine samples with various post treatments. All spectra are sharper than the raw sample and can be fitted well with two or three Lorentz lines. The fitting adjusted coefficient of determination (adj-$R^2$) for all spectra is higher than 0.995. The samples are denoted according to the etching time and the annealing temperature ($T_A$). For example, "N3-390" marks the sample with 30 min of etching time and 390 °C of $T_A$. The spectra for N4 and N6 series are fitted with 2 peaks, while N3 series requires 3 peaks to get a good fit ($R^2 > 0.995$). An additional peak in N3 series could be related to the complex composition of surface due to the insufficient time of acid treatment. N4 and N6 samples show a consistent evolution of FMR spectrum with increasing $T_A$. According to a literature [15], the annealing of amorphous ribbon could induce internal stress, resulting into an orthogonal configuration of bulk and surface magnetic anisotropy. Therefore, the peak with a higher (lower) intensity is assigned to the bulk (surface) mode. As $T_A$ increases, the intensity of surface mode is greatly suppressed. At 410 °C annealing, the surface mode becomes very broad, suggesting the surface magnetic anisotropy reduces and becomes non-uniform. The bulk mode of N6-series has a relatively narrower linewidth compared with N4-series, indicating a higher magnetic uniformity in bulk.

The $H_r$ of the bulk mode is plotted against $T_A$ in Fig. 6(a) for all samples, showing a convergent tendency at $T_A$ = 410 °C, indicating the vanishing of $H_\sigma$ due to the release of internal stress. With the assumption that the $T_A$-induced variation of $M_s$ is negligible in this narrow $T_A$ range, the stress induced anisotropy field is calculated and plot in Fig. 6(b) using Eq. (1) with $M_s$ = 1407, 1415 and 1411 emu/cm$^3$ for N3-, N4- and N6-series, respectively. $N_d$ is calculated [16] as 3.3π according to the sample geometry. For N6-series, $H_\sigma$ deceases with increasing $T_A$, in agreement with the report on FeCoB metallic glass [17]. At $T_A$ = 370 °C, the $H_\sigma$ is 40 Oe, −35 Oe and −74 Oe for N6, N4 and N3 respectively. The positive sign indicates the easy axis of bulk coincides with the ribbon axis, instead of the $H_A$ direction. Along with the result in Fig. 2, it implies that the long acid treatment could modify the surface composition and consequently the $H_\sigma$. It is interesting to observe that the direction of annealing-induced stress is reversed with changing the acid treatment time.

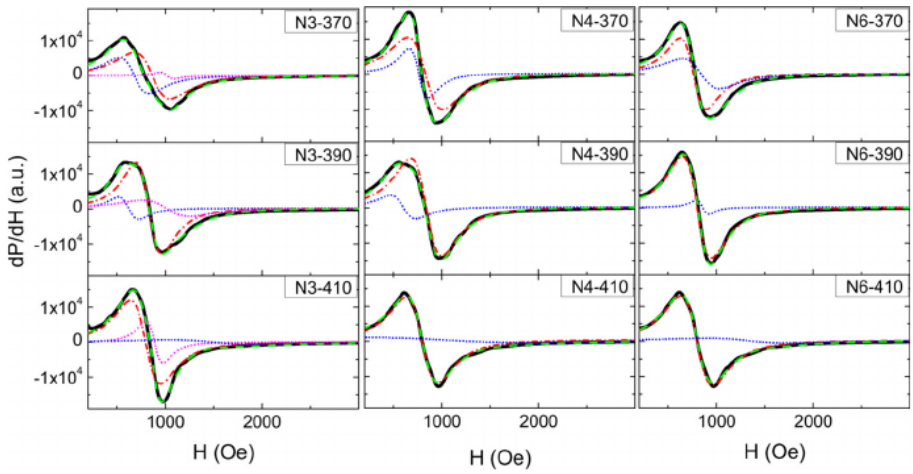


**Fig. 5.** Solid curves are the derivated FMR spectra for annealed samples. Each spectrum is fitted with two to three Lorentz functions, including the major (dash dot line) and the minor mode (dot lines). Dash lines are the cumulative curve of major and minor modes for each fitting.

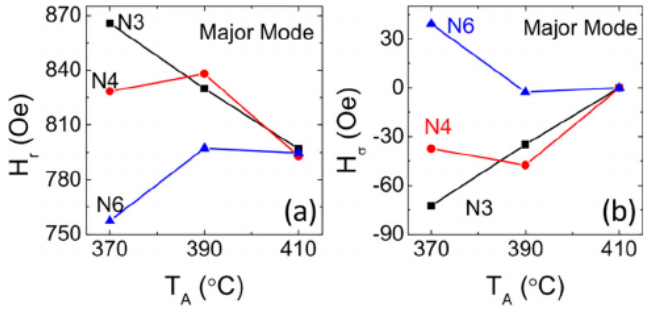


**Fig. 6.** The dependency of (a) $H_r$ and (b) $H_\sigma$ of major mode on $T_A$. The squares, circles and triangles are results for N3, N4 and N6 acid treatments, respectively. Lines are for eye-guiding. Data in (a) and (b) are strongly correlated. In (b), $H_\sigma$ merges to the same value near zero at = 410 °C for all three samples, indicating a relaxation of anisotropy field at a critical temperature.

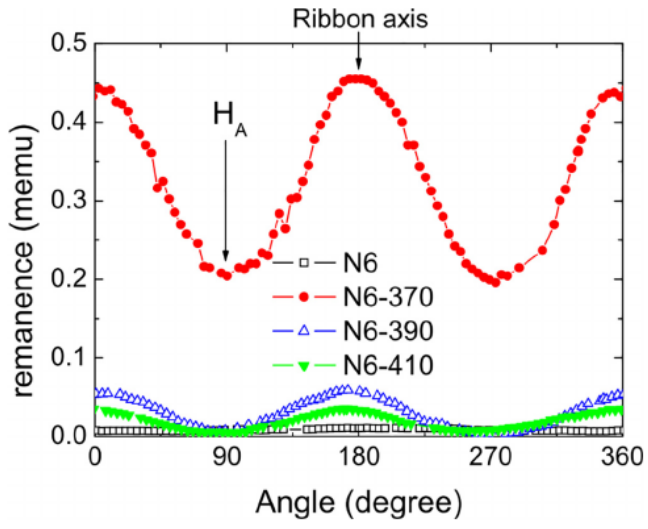


**Fig. 7.** The squares, circles, up-triangles and down-triangles are angular dependent remnant for N6, N6-370, N6-390 and N6-410, respectively. Lines are for eye-guiding. 0 and 180° are the direction of ribbon axis. The in-plane magnetic field during annealing is applied along 90°.

To confirm the change of in-plane magnetic anisotropy with annealing temperature, the angular dependent remanence R(θ) for N6 series is plotted in Fig. 7. The θ angle is defined as the deviation of the direction of applied field from the long axis of ribbon on the surface plane. N6 shows a very low ($\sim 10^{-6}$ emu) remanence in all directions, implying a low magnetic anisotropy before annealing. After annealing at 370 °C, the remanent magnetizations for all directions are enhanced. With further increasing $T_A$ to 390 and 410 °C, the remanent magnetization as well as the magnetic anisotropy is suppressed due to the relaxation of internal stress. The in-plane magnetic anisotropy defined as R(0)-R(90) is 0.204, 0.054 and 0.030 memu for N6-370, N6-390 and N6-410 respectively. Furthermore, R(0) is always larger than R(90) for annealed samples, suggesting the overall easy axis is along the ribbon axis, in agreement with the FMR result. The result of angular dependent remanence on the N6 series samples is consistent with that of FMR, suggesting 370 °C is the optimal annealing temperature to produce a large bulk magnetic anisotropy for the surface clean ribbons.

## 5. Conclusion

The magnetic anisotropy of amorphous $Fe_{67}Co_{10}Cr_3Si_5B_{15}$ ribbons with acid and heat treatments are studied with VSM magnetometer and FMR technique. FMR spectra are found to be more effective than M-H loops to detect the surface precipitate and it could also distinguish the surface magnetic anisotropy from the bulk one. The bulk magnetic anisotropy field has a positive value of 40 Oe at $T_A$ = 370 °C for the long acid treated sample, but it converts to near zero for all samples at $T_A$ = 410 °C due to the relaxation of internal stress. For acid-etching effect, it is found that the acid treatment does not only remove surface precipitates, but also modify the surface composition which affects the annealing-induced magnetic anisotropy. This work demonstrates FMR is a highly effective technique to correlate the post-treatment conditions with the configuration of magnetic anisotropy in magnetic amorphous ribbons.

## Acknowledgements

This work is financially supported in part by the Ministry of Science and Technology of R. O. C. under the projects of MOST106-2811-M-002-092 and MOST 105-2112-M-002-010-MY3; and also in part by the Goszadanie of Russian Federation (Project No. 3.1941.2017/PCh). The author (J. G. Lin) is grateful to Prof. S. Y. Huang (Physics Department, National Taiwan University, Taiwan) for providing VSM facility.

## References


[1] C. Suryanarayana, A. Inoue, Iron-based bulk metallic glasses, Int. Mater. Rev. 58 (3) (2013) 131–166.

[2] D.C. Hofmann, Bulk metallic glasses and their composites: a brief history of diverging fields, J. Mater. 2013 (2013) 1–8.

[3] A. Inoue, B.L. Shen, C.T. Chang, Fe- and Co-based bulk glassy alloys with ultrahigh strength of over 4000MPa, Intermetallics 14 (8–9) (2006) 936–944.

[4] P. Butvin et al., Field annealed closed-path fluxgate sensors made of metallic-glass ribbons, Sens. Actuators A 184 (2012) 72–77.

[5] H.S. Chen, S.D. Ferris, E.M. Gyorgy, H.J. Leamy, R.C. Sherwood, Field heat treatment of ferromagnetic metallic glasses, Appl. Phys. Lett. 26 (7) (1975) 405–406.

[6] P. Jia, E.-G. Wang, The effects of high magnetic field annealing on the structural relaxation of Fe71(Nb0.8Zr0.2)6B23 bulk metallic glass, Mater. Res. 18 (suppl 1) (2015) 40–43.

[7] N.A. Skulkina, O.A. Ivanov, E.A. Stepanova, L.N. Shubina, P.A. Kuznetsov, A.K. Mazeeva, Mechanisms of the magnetic properties improvement of amorphous soft magnetic Fe- and Co-based alloys as a result of the in-air heat treatment, Phys. Proc. 82 (2016) 69–77.

[8] J.E. Velasco, A. Concustell, E. Pineda, D. Crespo, Plastic deformation induced anisotropy in metallic glasses: a molecular dynamics study, J. Alloy. Compd. 707 (2017) 102–107.

[9] Q. Luo, B. Schwarz, N. Mattern, J. Shen, J. Eckert, Roles of hydrogenation, annealing and field in the structure and magnetic entropy change of Tb-based bulk metallic glasses, AIP Adv. 3 (3) (2013) 032134.

[10] N.A. Skulkina, O.A. Ivanov, E.A. Stepanova, I.O. Pavlova, Effect of electrolytic oxidation and hydrogenation on the magnetization distribution and magnetic properties of ribbons of amorphous soft magnetic iron-based alloys, Phys. Metals Metallogr. 111 (5) (2011) 458–463.

[11] A. Slawskawaniewska, A. Siemko, J. Finkfinowicki, L. Zaluski, H.K. Lachowicz, Some aspects of simultaneous stress-annealing and field-annealing of metallic glasses, J. Magn. Magn. Mater. 101 (1–3) (1991) 40–42.

[12] H.K. Lachowicz et al., Tailoring soft and hard magnets by annealing Co-based metallic glass, J. Magn. Magn. Mater. 190 (3) (1998) 267–276.

[13] A.J. Kailath, A. Kumar, A. Mitra, Effect of metalloids on crystallization and magnetic behaviour of FeCoSiB based metallic glass, Bull. Mater. Sci. 29 (2) (2006) 127–131.

[14] K. Freitas, J. Toledo, L. Figueiredo, P. Morais, J. Felix, C. de Araujo, Static and dynamic magnetization investigation in permalloy electrodeposited onto high resistive N-type silicon substrates, Coatings 7 (2) (2017) 33.

[15] H.N. Ok, A.H. Morrish, Origin of the perpendicular anisotropy in amorphousFe82B12Si6ribbons, Phys. Rev. B 23 (5) (1981) 2257–2261.

[16] A. Aharoni, Demagnetizing factors for rectangular ferromagnetic prisms, J. Appl. Phys. 83 (6) (1998) 3432–3434.

[17] J.M. Barandiarán, J. Gutiérrez, Z. Kaczkowski, D. De Cos, Influence of annealing temperature on the magnetic and magnetoelastic properties in Fe–Co–B metallic glasses, J. Non-Cryst. Solids 329 (1–3) (2003) 43–47.

Superconductor Science and Technology

**PAPER**

# Microwave-assisted synthesis and critical analysis for $YBa_2Cu_3O_{6+\delta}$ nanoparticles

To cite this article: Ashish Chhaganlal Gandhi and Jauyn Grace Lin 2018 *Supercond. Sci. Technol.* **31** 055002

IOP Publishing Superconductor Science and Technology
Supercond. Sci. Technol. 31 (2018) 055002 (8pp) https://doi.org/10.1088/1361-6668/aab0c5

# Microwave-assisted synthesis and critical analysis for $YBa_2Cu_3O_{6+\delta}$ nanoparticles

**Ashish Chhaganlal Gandhi and Jauyn Grace Lin**

Center for Condensed Matter Science, National Taiwan University, Taipei 10617, Taiwan

E-mail: jglin@ntu.edu.tw

Received 20 December 2017, revised 12 February 2018
Accepted for publication 20 February 2018
Published 23 March 2018

**Abstract**

A new cost effective scheme of a microwave-assisted sol–gel route followed by a short annealing time is proposed to synthesize YBCO nanoparticles (NPs) of various sizes. The advanced techniques of synchrotron radiation x-ray diffraction (SRXRD) and electron spin resonance (ESR) are used to analyze the size effects on their magnetic/superconducting properties. The major interesting finding is that the size of YBCO NPs could confine the amount of oxygen content and consequently change the superconducting transition temperature ($T_C$) of YBCO NPs. The ESR result demonstrates a sensitive probe to characterize surface defects in the oxygen-deficient YBCO NPs.

Keywords: YBCO, superconductivity, oxygen occupancy, microwave synthesis, ESR

(Some figures may appear in colour only in the online journal)

## 1. Introduction

The world's first high-temperature superconductor $YBa_2Cu_3O_{6+\delta}$ (YBCO-$\delta$) with a superconducting transition temperature ($T_C$) of 93 K, which is above the boiling point of liquid nitrogen (73 K), was discovered in 1987 [1]. The discovery of YBCO made the applications of the superconductor costless and operationally effective. However, the superconducting and electrical properties of YBCO critically depend on the excess oxygen content ($\delta$), which requires a considerable effort to detect and control. The excess oxygen induces a structural transformation from tetragonal ($0 \leqslant \delta \leqslant 0.35$) to orthorhombic ($\delta > 0.35$) with a charge redistribution along the $c$-axis [2], leading to the generation of hole carriers in the $a$–$b$ plane and the occurrence of superconductivity. Numerous studies have been carried out to understand the effects of $\delta$ on the physical properties of bulk YBCO, but only a few for YBCO nanoparticles (NPs) [3–13]. It is known that the physical properties of YBCO NPs depend on the particles size and surface defects associated with the synthesis methods [14]. However, the correlation between size, $\delta$, and superconducting properties of NPs is rarely studied because of the lack of proper tools. The electron spin resonance (ESR) spectrometer is one of the sensitive probes to study the oxygen concentration by detecting the free electron of the $Cu^{2+}$ ions of the YBCO system [15]. Fully oxygenated YBCO bulk is ESR-silent due to the non-magnetic ground state or excessive line broadening [16, 17]. On the contrary, the mechanically grounded powders of YBCO are ESR-active, which is attributed to either the interaction between Cu ions in the chain ($Cu(2)O_5$ clusters) and those in the plane ($Cu(1)O_5$ cluster) [17], or a parasitic phase (e.g. $Y_2BaCuO_5$ and $BaCuO_{2+x}$) [15].

In the past, various wet chemical methods such as the soft chemical approach [13], citrate-gel [8], and citrate pyrolysis [9, 10, 12] were often used for the synthesis of YBCO NPs. Alternatively, a physical method such as microwave heating could be effective, but is less discussed [18]. The principle of microwave heating is to vibrate the electric dipoles of molecules with an electric field, resulting in a uniform heat transfer in the materials. Therefore, within a short period of time, the CuO molecule could be heated up to 550 °C by absorbing microwave radiation of 2.45 GHz to provide the energy required to form the phase of YBCO [19–22]. In this work, we propose a microwave-assisted sol–gel synthesis, followed by a short annealing time in an ambient atmosphere, to prepare size-controllable YBCO NPs. This new experimental route reduces the synthesis steps as well as the synthesis time. For a critical analysis, we use advanced probes, synchrotron radiation x-ray diffraction (SRXRD) and ESR, to obtain detailed structural and oxygen properties. Our result displays an unusual size dependency of

 

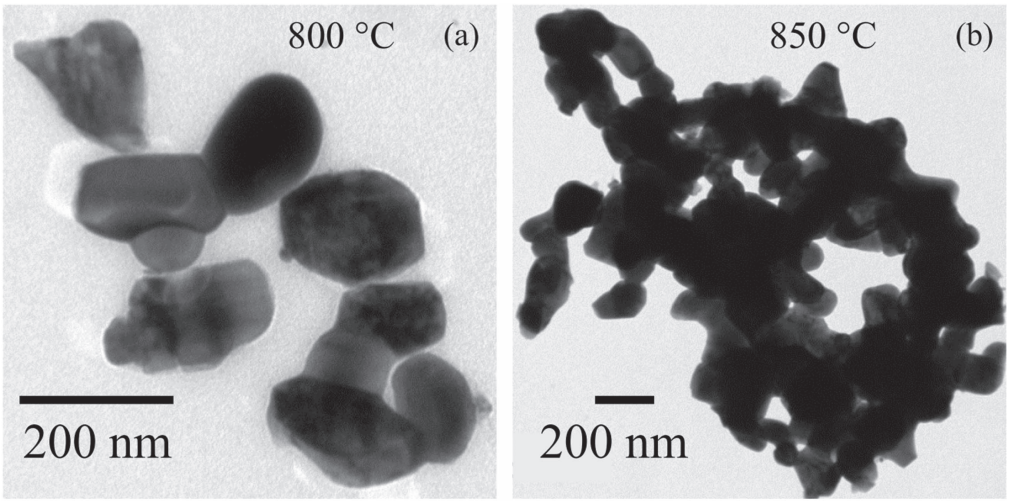


**Figure 1.** (a) and (b) show the TEM images of 800 °C and 850 °C annealed samples, respectively.

$T_C$ and the lattice parameter, which is correlated with a combined effect of hole doping and size confinement.

## 2. Material synthesis and experimental methods

### 2.1. Chemicals

Yttrium nitrate hexahydrate ($Y(NO_3)_3 \cdot 6H_2O$) (99.9%, Alfa Asear), barium nitrate ($Ba(NO_3)_2$) (99.95%, Alfa Asear), copper nitrate trihydrate ($Cu(NO_3)_2 \cdot 3H_2O$) (99%, Across), citric acid ($C_6H_8O_7$) (99.5 + %, Alfa Asear), and 25% $NH_4OH$ (Sigma Aldrich) are used. Deionized water (DIW) is used as a solvent.

### 2.2. Synthesis of $Y_1Ba_2Cu_3O_{6+\delta}$ NPs

A typical sol–gel method for the synthesis of $Y_1Ba_2Cu_3O_{7-\delta}$ NPs is as follows: 1.915 g of $Y(NO_3)_3 \cdot 6H_2O$, 2.613 g of $Ba(NO_3)_2$, and 3.624 g of $Cu(NO_3)_2 \cdot 3H_2O$ are dissolved in 400 ml DIW, and 6.724 g of citric acid in 200 ml DIW water, separately. To form a uniform solution, continuous magnetic stirring is employed at room temperature for 30 min. Then, the citric acid solution is added dropwise at a rate of 2 ml $min^{-1}$ to the nitrate solution under continuous magnetic stirring. A pH equal to 3 is set at room temperature by using 25% $NH_4OH$. Then, the solution is exposed to a 2.45 GHz frequency at 60% power of 800 W by using a domestic microwave oven (SHART R-T20Z) for 25 min, which results in the formation of a greenish-black colored powder. The above-formed powders are then dissolved in DIW, sonicated, and re-exposed to microwave using the same microwave condition for another 25 min, which results in the formation of black colored powders. Powders are ground and used as a precursor for the preparation of different sized NPs. The post annealing temperature $T_A$ is set as 750 °C, 800 °C, 850 °C, 920 °C, 950 °C, and 980 °C, with a duration of 2 h in air. The annealing of the precursor is carried out in a quartz tube furnace (Lindberg/Blue M, Model: TF55035A) with a heating and cooling rate of 5 °C $min^{-1}$.

### 2.3. Characterization techniques

Morphological analysis of the samples was carried out by using transmission electron microscopy (TEM) (Hitachi H-7100 operating at 200 kV). SRXRD measurements were performed at the National Synchrotron Radiation Research Center (Hyogo, Japan), Spring-8 contract beamline BL12B2, using a Rayonix MS225 (CCD) detector. The incident wavelength is 0.688 98 Å (18 keV), and the sample-to-detector distance is 149.4 mm. The measurements of temperature-dependent zero-field-cooled (ZFC) and field-cooled (FC) magnetization were carried out by using a quantum designed MPMS VSM SQUID magnetometer. The room temperature ESR spectra were taken using an X-band Bruker EMX system, and were recorded by placing powders into a quartz tube and then inserting it into a $T_{102}$ rectangular cavity. During ESR measurements, the frequency was kept constant at 9.44 GHz, while the magnetic field H was varied from 100 to 7000 Oe with a step of 5 Oe.

## 3. Experimental results

### 3.1. Morphology and structural analysis

Figures 1(a) and (b) show the typical TEM images for 800 °C and 850 °C annealed samples, respectively. The particles of the 800 °C sample are well separated, with the size varying from ~50 nm to 200 nm. Annealing at 850 °C results in the segregation of NPs. Annealing at and above 920 °C leads to a partial melting of YBCO, and a broad size distribution with non-uniform morphologies; this is consistent with the findings of previous reports [23–25]. Figure 2(a) shows the SRXRD spectra for 800 °C, 850 °C, 920 °C, 950 °C, and 980 °C annealed samples (bottom to top; spectra are shifted vertically for clarity). According to the data (symbols) and the fits with Rietveld refinement (solid lines), the structures of YBCO with $T_A > 800$ °C are all orthorhombic with the space group of Pmmm; meanwhile, the structure of the 750 °C sample is tetragonal (not shown here). The minor impurity phases such

**Table 1.** Summary of the SRXRD fitting parameters ($\delta$ = occupancy at the O(1) site, lattice constants, wRp, Rp, and $\chi^2$) for YBCO NPs along with the reported values of orthorhombic (*) and tetragonal (#) YBCO bulks for comparison [2].

| $\langle d \rangle$ (nm) | $\delta$ | $a$ | $b$ | $c$ | $wRp$ | $Rp$ | $X^2$ |
|---|---|---|---|---|---|---|---|
| 30 | 0 | 3.8766(9) | = a | 11.5926(29) | 0.1787 | 0.1174 | 193.8 |
| 34 | 0.35 | 3.8567(4) | 3.8820(4) | 11.6344(15) | 0.0611 | 0.0352 | 0.6981 |
| 39 | 0.75 | 3.8246(4) | 3.8780(5) | 11.6482(18) | 0.0680 | 0.0433 | 1.089 |
| 42 | 0.71(5) | 3.8172(1) | 3.8798(2) | 11.6711(6) | 0.0391 | 0.0257 | 0.1940 |
| 44 | 0.73(6) | 3.8163(1) | 3.8809(1) | 11.6812(5) | 0.0204 | 0.0146 | 0.0179 |
| 45 | 0.64(4) | 3.8161(1) | 3.8813(1) | 11.6809(5) | 0.0235 | 0.0165 | 0.0277 |
| *Bulk | 0.73 | 3.8275(1) | 3.8875(1) | 11.7063(2) | — | — | — |
| #Bulk | 0.09 | 3.8600(1) | = a | 11.8162(2) | — | — | — |

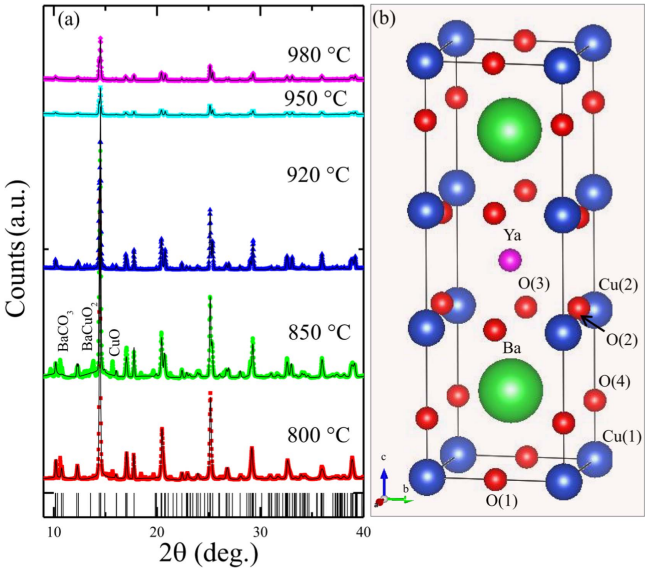


**Figure 2.** (a) Room temperature SRXRD spectra for the annealed samples with $T_A$ = 800 °C to 980 °C. SRXRD spectra are shifted vertically for clear visibility. (b) A unit cell of orthorhombic YBCO.

as $BaCO_3$ (orthorhombic, Pmcn) [26] is present for $T_A$ = 800 °C and 850 °C; $BaCuO_2$ (cubic, Im-3m) [27] and CuO (monoclinic, C2/c) [28] are present for $T_A$ = 800 °C–920 °C. The most intensive peak located at $2\theta \sim 15.54°$ is fitted with a Lorentzian function, and its full-width-at-half-maximum (FWHM) is determined [29]. The FWHM values decrease from $0.111 \pm 0.002°$ to $0.084 \pm 0.002°$ as $T_A$ increases from 750 °C to 980 °C. The size of the YBCO NP is calculated using Scherrer's formula: $\langle d \rangle = k\lambda/\beta \cos\theta$, where $\theta$ is the diffraction angle, $\beta$ is the FWHM, $\lambda$ an incident wavelength (= 0.068 898 nm), and $k$ is the Scherrer constant (= 0.94). The $\langle d \rangle$ value for $T_A$ = 750 °C, 800 °C, 850 °C, 920 °C, 950 °C, and 980 °C is 30, 34, 39, 42, 44, and 45 nm respectively. The increase of $\langle d \rangle$ with increasing annealing temperature is consistent with what was observed in the YBCO NPs synthesized by citrate pyrolysis [10].

The structural parameters, including oxygen site occupancy, are determined by using the Rietveld refinement for SRXRD patterns with GSAS software package [30, 31]. The sites of Y, Ba, Cu(1), Cu(2), O(2), O(3), and O(4) in a YBCO unit cell are demonstrated in figure 2(b) for a phase of full oxygen stoichiometry ($\delta$ = 1). To obtain the amount of oxygen content using the refinement method, the occupancies are constrained at their ideal values except for the oxygen occupancy at the O(1) site, the atomic positions (x, y, z) of all elements, and the lattice parameters ($a$, $b$, $c$). The structural parameters for YBCO NPs are summarized with a comparison of previous data in table 1, including $\delta$ (the occupancy at the O(1) site), lattice constants, wRp, Rp, and $\chi^2$.

### 3.2. Superconducting properties

In order to determine $T_C$ of NPs, the temperature-dependent magnetization M($T$) is measured from 2 K to 100 K at 10 Oe, with both ZFC and FC modes. Figures 3(a)–(c) are the M($T$) curves for selected samples 34, 39, and 42 nm in size. The value of $T_C$ is defined as the onset of the superconducting transition, as indicated with arrows. Compared to bulk YBCO, a relatively broad transition is observed in all NPs due to the surface defects [32]. In figure 3(a), the ZFC curves of the 34 nm sample show a negative M from 100 K to ~20 K, which is attributed to the diamagnetic signal of $BaCO_3$ [33]. In particular, the ZFC (FC) curve shows a sharp drop (rise) at ~14 K, and a rise (drop) at ~10 K. The first transition temperature at 14(2) K is assigned to the $T_C$ of YBCO, and is close to the reported value for YBCO-0.35 [2]. With increasing the size from 34 to 42 nm, $T_C$ shifts drastically from 14(2) to 90(2) K. The observed transition at ~10 K is assigned to the Neel transition temperature ($T_N$) of the antiferromagnetic $BaCuO_2$ impurity phase [34], which manifests as the bump in the FC–M($T$) curves of the 39 nm sample. The strength of magnetic shielding of the superconductor is quantified by the negative value of magnetization at 2.4 K, which increases with increasing size, and reaches a maximum value of 0.45 emu $g^{-1}$ at 42 nm. The M($H$) curves at T = 300 K with H = ± 10 kOe are shown in the inset of figure 3(b) for 34, 39, and 42 nm NPs. A weak hysteresis loop is observed for all three samples, which is assigned to the intrinsic defects such as oxygen vacancies residing on the surface of NPs [7–10, 12].

### 3.3. ESR analysis

ESR is a powerful tool for investigating unpaired electrons in transition metal oxides [26]. In principle, a paramagnetic

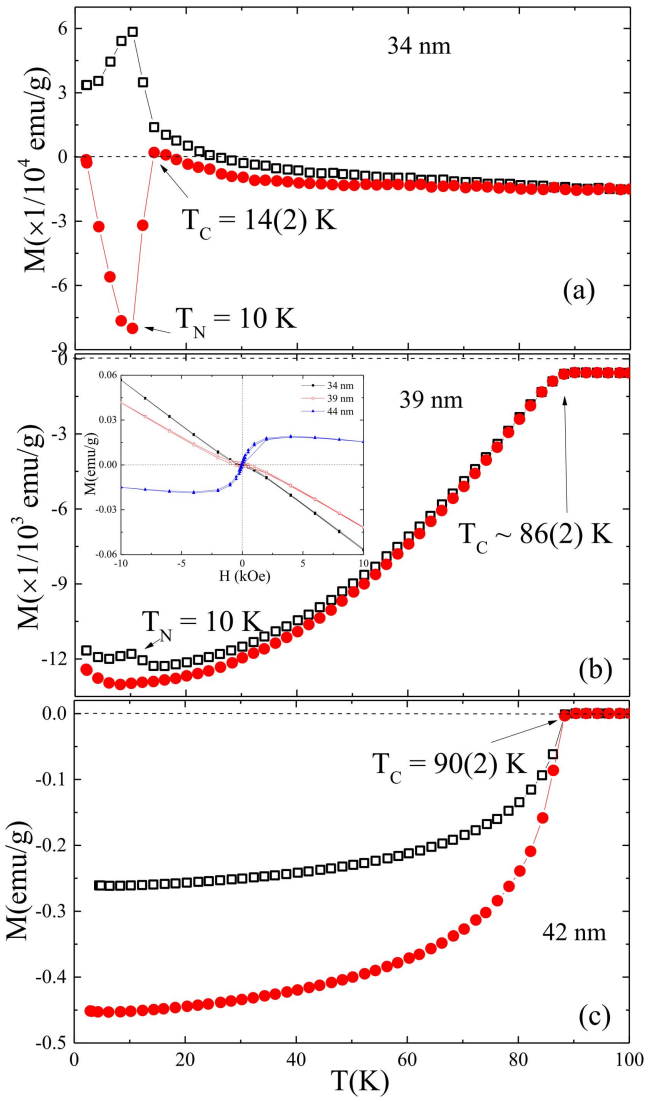


**Figure 3.** (a)–(c) Temperature dependent magnetization M(*T*) measured using the ZFC–FC process with a 10 Oe field for 34, 39, and 42 nm NPs. The inset of (b) shows the M(H) loop measured at 300 K for 34, 39, and 42 nm NPs.

sample is placed in a uniform magnetic field that splits the energy levels of the ground state by $\Delta E$. $\Delta E = g\beta H_r = h\nu$, where $\nu$ is the microwave frequency, $h$ is the Planks constant, $\beta$ is the Bohr magnetron, $H_r$ is the resonance field, and g is the gyromagnetic ratio of the free electron and is equal to 2.002. The spins of unpaired electrons rotate (so called precession) with the same frequency as the applied microwave when a resonance condition occurs. The value of $H_r$ is used to calculate the g-factor, and the line-width ($\Delta$H) represents the relaxation rate of spins. The amplitude (A) of the ESR spectrum is proportional to the concentration of unpaired electrons. The room temperature first-derivative ESR spectra as a function of *H* for 34, 39, and 42 nm samples are shown in figure 4 (top to bottom). Three characteristic features are observed: (i) the intensity of ESR spectra increases with the increase of particle size, and is ascribed to an increase in the concentration of paramagnetic complexes; (ii) the ESR peak at the low absorption field disappears in the 42 nm sample;

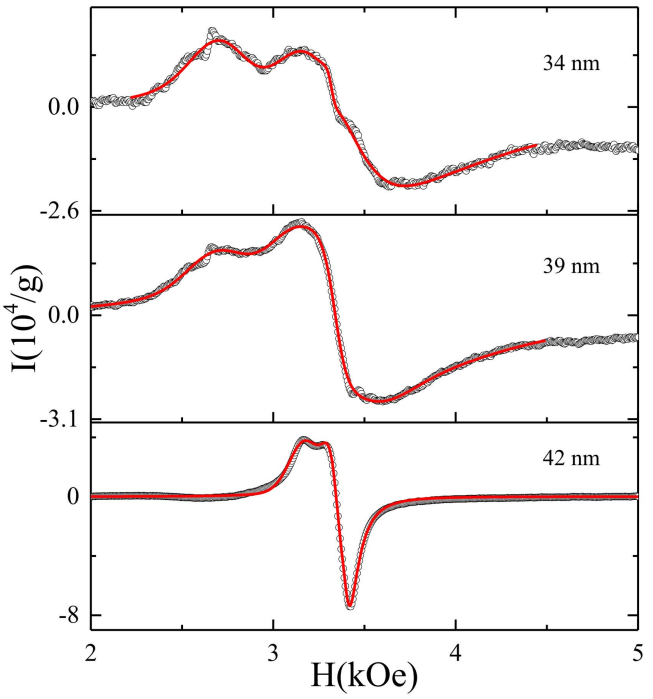


**Figure 4.** Room temperature first-derivative ESR absorption spectra of 34, 39, and 42 nm NPs (from top to bottom), where the solid line is the best fit obtained by deconvoluting the ESR spectrum using a sum of Gaussian and Lorentzian functions.

and (iii) the peak splitting near the free spin resonance field (Hr ~ 3374 Oe) becomes more pronounced in the 42 nm sample.

Figure 5(a) is the ESR spectrum for the 39 nm NP. The spectrum is deconvoluted using a sum of two Gaussian and two Lorentzian differential functions (represented by dashed and dotted lines, respectively). The deconvolution expression can be written as follows:

$$I = I_o - \frac{4}{\sqrt{\pi/2}}\left[\frac{A_1(H-H_{r1})}{\Delta H_1^3}e^{-2\frac{(H-H_{r1})^2}{\Delta H_1^2}} + \frac{A_2(H-H_{r2})}{\Delta H_2^3}e^{-2\frac{(H-H_{r2})^2}{\Delta H_2^2}}\right] - \frac{16}{\pi}\left[\frac{A_3\Delta H_3(H-H_{r3})}{(4(H-H_{r3})^2+\Delta H_3^2)^2} + \frac{A_4\Delta H_4(H-H_{r4})}{(4(H-H_{r4})^2+\Delta H_4^2)^2}\right],$$

where ($A_1$, $A_2$), ($H_{r1}$, $H_{r2}$), and ($\Delta H_1$, $\Delta H_2$) are the amplitude, resonance field, and line-width of the two Gaussian resonance peaks, and ($A_3$, $A_4$), ($H_{r3}$, $H_{r4}$), and ($\Delta H_3$, $\Delta H4$) are those of the two Lorentzian resonance peaks, respectively. Note that the best fit for 42 nm particles is obtained by using a sum of only one Gaussian and two Lorentzian differential functions. Figure 5(b) depicts the values of effective *g*-factors ($g_i$) calculated by $h\nu = \beta g_i H_{ri}$ (where $\nu$ = 9.44 GHz, and $i$ = 1, 2, 3, 4) with respect to particle size. The values of $g_1$, $g_2$, and $g_3$ decrease slightly with an increase of particle size from 34 to 39 nm, above which they show a similar value, whereas $g_4$

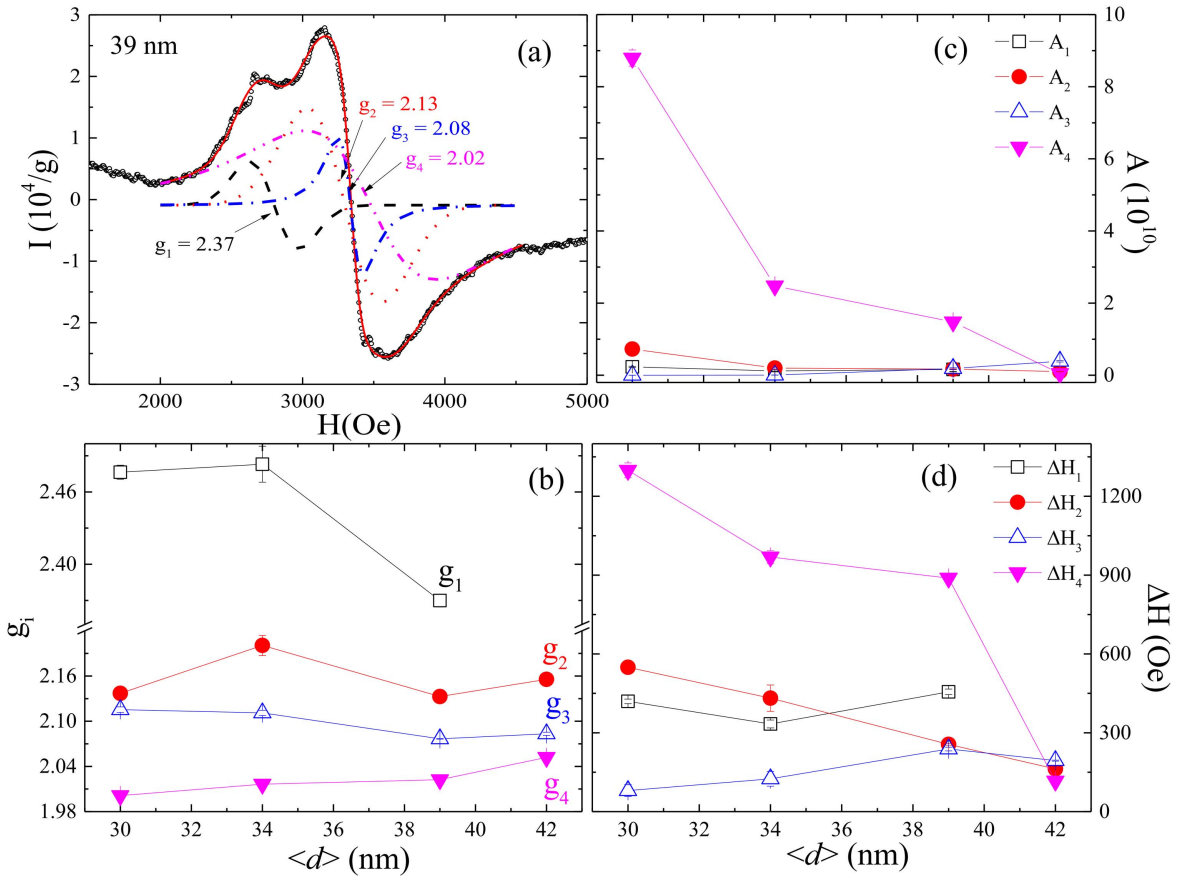


**Figure 5.** (a) Deconvoluted ESR spectra of 39 nm NPs using a sum of two Gaussian and two Lorentzian functions. Plot of size dependency of (b) effective g-factor, (c) amplitude, and (d) line-width of 34, 39, and 42 nm NPs.

shows a slight increment. The values of $g_i$ for different samples remain within a range: $g_1 = 2.48 \sim 2.37$ (open squares), $g_3 = 2.12 \sim 2.08$ (open right-side up triangles), $g_2 = 2.14 \sim 2.20$ (solid spheres), and $g_4 = 2.00 \sim 2.05$ (solid upside down triangles). Figures 5(c) and (d) show the size dependencies of $g_i$, $A_i$, and $\Delta H_i$. The values of $A_4$ and $\Delta H_4$ decrease dramatically with the increase of particle size, and show a sharp drop at 42 nm. Conversely, values of $A_i$ and $\Delta H_i$ with $i = 1, 2, 3$ do not show a significant size dependency.

## 4. Discussion

Recently, a complete diagonalization method and the perturbation theory method were used to calculate the axial g-tensor values ($g_{II}$, $g_{\perp}$) for the isolated tetrahedral $[CuO5]^{8-}$ complex of the tetrahedral YBCO [35]. Figure 6(a) shows $Cu(2)O_5$ complexes present in a tetragonal YBCO structure, where $g_{II}$ and $g_{\perp}$ are the g-factors along the Cu(2)——O(4) and Cu(2)——O(2) bonds, respectively. The reported experimental values of $g_{II} = 2.39$ and $g_{\perp} = 2.07$ from YBCO powder samples are close to the theoretical values summarized in the first and second rows of table 2. Based on the chain-plane-paramagnetic-center model [17], the breaking of Cu(2)——O(4) bonds results in an instability of the $3d^{10}$ state of Cu(1) in the Cu(1)——O(4) chain, inducing an electron transfer to the $3d^8$ state of Cu(2) in the $CuO_2$ plane, as shown in figure 6(b). The disturbance of charge equilibrium between chain and plane could result in the increase of paramagnetic complex axial g-tensors. For example, $g_{II} \sim 2.22$ and $g_{\perp} \sim 2.06$ for the orthorhombic YBCO with $\delta = 1.0$. In comparison with the overall ESR data for $Cu(2)O_5$ complexes, single crystal, and powder YBCO, the obtained $g_1$ and $g_3$ are assigned to the signal from the tetragonal YBCO phase, while $g_2$ and $g_4$ are from orthorhombic YBCO phase. It is an interesting finding that all measured NPs have coexisting tetragonal and orthorhombic phases.

However, a question remains unanswered: How does the size of YBCO NPs control the superconducting property? Since the surface defects result in broken Cu(1)——O(4) bonds, the large surface-to-volume ratio in a small NP could lead to an increase in oxygen vacancies (less oxygen content) [12], and thus $T_c$ decreases. Figure 7(a) plots the size-dependent structure parameters, superconducting transition, and oxygen content. A significant lattice contraction along the $a$-axis is observed. The $a$ decreases drastically from 3.8766 (11) Å to 3.8161(1) Å with the particle size increasing from 30 to 45 nm; meanwhile, $b$ (~3.88 Å) does not show a significant size dependency. Contrary to single crystal and bulk YBCO, in which the lattice parameter $c$ decreases with increasing oxygen content, $c$ increases from 11.5926(29) Å to 11.6809(5) Å with $\delta$ increasing from 0.35 to 0.73. This result

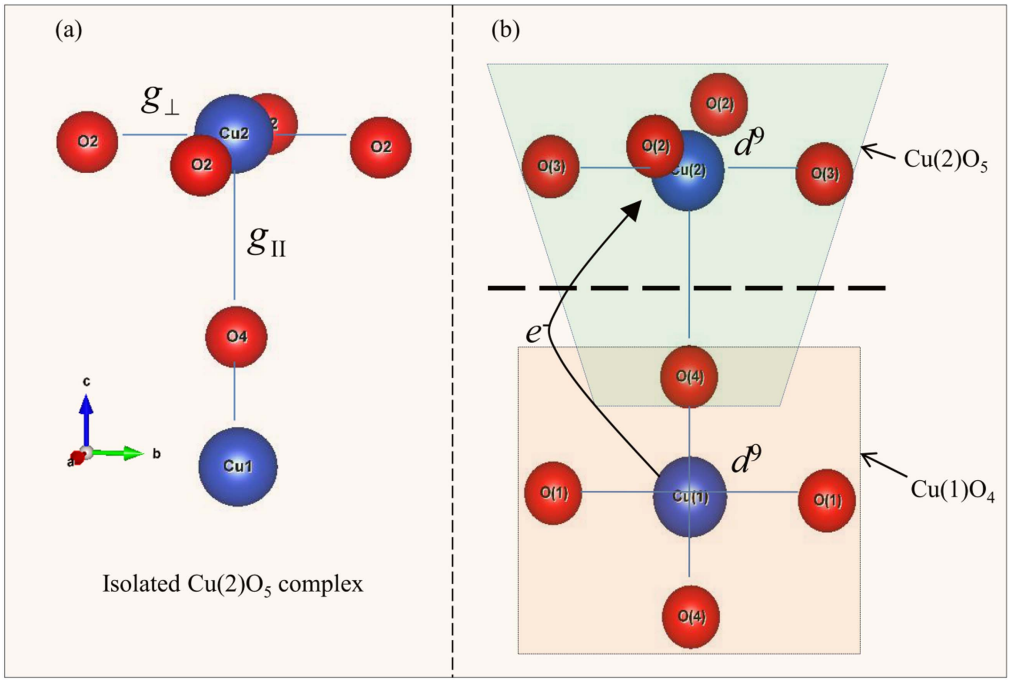


**Figure 6.** A schematic diagram for (a) $Cu(2)O_5$ complexes in the tetragonal YBCO structure along the *c*-axis, and (b) charge transfer between the $3d^{10}$ state of Cu(1) in the chain and the $3d^8$ state of Cu(2) in the plane of the orthorhombic YBCO structure along the *c*-axis.

**Table 2.** Summary of the g-factors for YBCO NPs along with the values from the literature, including those for the isolated $CuO_5$ complex (experiment and theory), ceramic, powder samples (PD), and single crystals (SC).

| Composition | $g_1(g\|\|)$ | $g_3(g_\perp)$ | $g_2(g\|\|)$ | $g_4(g_\perp)$ |
|---|---|---|---|---|
| Theory [35] | 2.405 | 2.056 | — | — |
| $CuO_5$ complex | 2.409 | 2.054 | — | — |
| PD, $\delta = 0.36$ (tetragonal) [17] | 2.39 | 2.07 | — | — |
| Ceramic (3 mm) | — | — | — | — |
| PD, $\delta = 1$ | — | — | 2.21 | 2.06 |
| PD, $\delta = 1$ [36] | — | — | 2.203 | 2.098 |
| SC, $\delta = 0.9$ [37] | — | — | 2.270 | 2.020 |
| PD, $\delta = 0.95$ [38] | — | — | — | $2.096(g_{av})$ |
| $\delta = 0.05$ | — | 2.096 | 2.218 | 2.040 |
| $\delta = 0.95$ | — | 2.116 | 2.225 | 2.045 |
| $0.35 \leqslant \delta \leqslant 0.45$ | — | 2.121 | 2.229 | 2.048 |
| SC, $\delta = 0.9$ | — | — | 2.270 | 2.020 |
| This work | | | | |
| NP, $\delta = 0$ | 2.476 | 2.115 | 2.137 | 2.001 |
| NP, $\delta = 0.35$ | 2.483 | 2.111 | 2.201 | 2.016 |
| NP, $\delta = 0.65$ | 2.370 | 2.077 | 2.132 | 2.022 |
| NP, $\delta = 0.71$ | — | 2.083 | 2.156 | 2.052 |

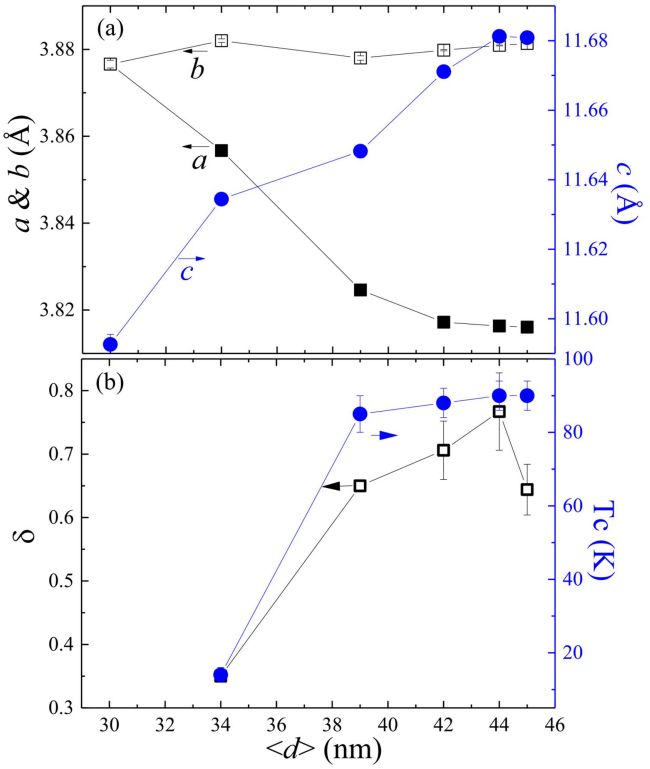


**Figure 7.** Plot of size dependencies of (a) lattice parameters and (b) oxygen occupancy at the O(1) site; $\delta$ values (left scale) and $T_C$ values (right scale).

suggests that the observed size dependencies of lattice parameters are mainly from the finite-size effect and less from the oxygen content. Figure 7(b) plots the $\delta$ (left) and the $T_C$ (right) vs. $\langle d \rangle$, indicating a similar trend of $T_C$ and $\delta$ with increasing particle size. The above results confirm that the oxygen content of the NP increases with increasing particle size, and thus $T_c$ is enhanced.

Another measure for the oxygen vacancies is the amplitude of the ESR. In general, the amount of vacancies is proportional to the amplitude of the ESR peak due to the increase of paramagnetic centers. In figure 5(c), the intensity

$A_4$ of the ESR peak shows a great reduction upon increasing the particle size, implying that oxygen vacancies are mainly on the $CuO_2$ plane. The observed reduction of $\Delta H_4$ for the 42 nm sample suggests that the distribution of oxygen vacancies is more uniform in the large NPs. As a consequence, $T_c$ is enhanced with increasing particle size. This study shows the advantage of utilizing the ESR technique for in-depth characterization of paramagnetic centers in oxygen-deficient complex compounds like YBCO NPs.

## 5. Conclusions

The crystalline and magnetic properties of microwave-assisted sol–gel-synthesized YBCO NPs (34 to 45 nm) were systematically investigated using SRXRD and ESR techniques. The finite-size effect leads to lattice contraction along the *c*-axis and expansion along the *a*-axis. A drastic rise in $T_C$ from 14(2) K to 90(2) K is correlated with the increase in oxygen occupancy at the O(1) site in the $a-b$ plane. At room temperature, ESR spectra reveal four peaks with effective g-factors of $g_1 = 2.48 \sim 2.37$, $g_2 = 2.14 \sim 2.20$, $g_3 = 2.12 \sim 2.08$, and $g_4 = 2.00 \sim 2.05$. The ($g_1$, $g_3$) and ($g_2$, $g_4$) peaks are assigned to the axial g-tensor ($g_{II}$, $g_{\perp}$) of isolated $Cu(2)O_5$ and chain-plane-paramagnetic complex, respectively. The amplitude of the ESR peak with $g = 2.05$ significantly decreases with increasing particle size, reflecting a reduction of oxygen vacancies in the $CuO_2$ plane. Our finding shows a correlation between particle size and oxygen vacancies within the finite sizes.

**Notes**

The authors declare no competing financial interest.

## Acknowledgments

This work is partly supported by the National Taiwan University through project number NTU-104R4000 Ashish Chhaganlal Gandhi (ACG), and partly supported by the Ministry of Science and Technology at Taiwan via project number MOST 105-2112-M-002-010-MY3 Jauyn Grace Lin (JGL).

## ORCID iDs

Ashish Chhaganlal Gandhi https://orcid.org/0000-0002-1900-8702

## References

[1] Wu M K, Ashburn J R, Torng C J, Hor P H, Meng R L, Gao L, Huang Z J, Wang Y Q and Chu C W 1987 Superconductivity at 93 K in a new mixed-phase Y-Ba-Cu-O compound system at ambient pressure *Phys. Rev. Lett.* **58** 908–10

[2] Jorgensen J D, Veal B W, Paulikas A P, Nowicki L J, Crabtree G W, Claus H and Kwok W K 1990 Structural properties of oxygen-deficient $YBa_2Cu_3O_{7-d}$ *Phys. Rev.* B **41** 1863–77

[3] Blinov E, Fleisher V G, Huhtinen H, Laiho R, Lähderanta E, Paturi P, Yu P S and Vlasenko L 1997 Preparation of one to three unit cell thick $YBa_2Cu_3O_{7-x}$ powders and investigation of their magnetic and microwave properties *Supercond. Sci. Technol.* **10** 818

[4] Khene S, Gasmi M and Fillion G 2015 Phase transition in $YBa_2Cu_3O_{7-\delta}$ and $YBa_2Cu_3O_{7-\delta}/Y_3Fe_5O_{12}$ nanoparticles at low temperatures and high fields *J. Magn. Magn. Mater.* **373** 188–94

[5] Gasmi M, Khene S and Fillion G 2013 Coexistence of superconductivity and ferromagnetism in nanosized YBCO powders *J. Phys. Chem. Solids* **74** 1414–8

[6] Khene S, Gasmi M and Fillion G 2011 Detailed elaboration method and magnetic study of nanometrical YBCO/YIG system *J. Supercond. Nov. Magn.* **24** 427–35

[7] Fan W, Zou L-J and Zeng Z 2013 Ferromagnetism on surface of $YBa_2Cu_3O_7$ particle *Physica C* **492** 80–9

[8] Arabi H, Jamshidi S, Komeili M and Amirabadizadeh A 2013 Coexistence of superconductivity and ferromagnetic phases in YBa2Cu3O7$-\delta$ nanoparticles *J. Supercond. Nov. Magn.* **26** 2069–71

[9] Zhu Z, Gao D, Dong C, Yang G, Zhang J, Zhang J, Shi Z, Gao H, Luo H and Xue D 2012 Coexistence of ferromagnetism and superconductivity in YBCO nanoparticles *Phys. Chem. Chem. Phys.* **14** 3859–63

[10] Hasanain S K, Akhtar N and Mumtaz A 2011 Particle size dependence of the superconductivity and ferromagnetism in YBCO nanoparticles *J. Nanopart. Res.* **13** 1953–60

[11] Topal U 2010 Unexpected transport and magnetic properties in Y–Ba–Cu–O superconductors *Phys. Status Solidi* A **207** 1196–203

[12] Shipra A, Gomathi A, Sundaresan A and Rao C N R 2007 Room-temperature ferromagnetism in nanoparticles of superconducting materials *Solid State Commun.* **142** 685–8

[13] Shen Z, Hu Y, Fei L, Li K, Chen W, Gu H and Wang Y 2015 Photocatalytically active $YBa_2Cu_3O_{7-x}$ nanoparticles synthesized via a soft chemical route *J. Nanomater.* **2015** 5

[14] Gazquez J *et al* 2016 Emerging diluted ferromagnetism in high-Tc superconductors driven by point defect clusters *Adv. Sci.* **3** 2198–3844

[15] de Mesquita R N *et al* 1989 ESR experiments and spectra simulations in $YSa_2Cu_30_7$, $Y_2SaCu_{05}$, and $SaCuO_{2+x}$ *Phys. Rev.* B **39** 6694–9

[16] Deville A, Gaillard B, Noël H, Potel M, Gougeon P and Levet J C 1989 ESR of YBa2Cu3O7 single crystals : on the nature of the magnetic centres *J. Phys. France* **50** 2357–74

[17] Stankowski J, Hilczer W, Baszyński J, Czyżak B and Szczepańska L 1991 EPR of complex paramagnetic center in $YBa_2Cu_3O_{7-\gamma}$ induced and suppressed by mechanical processing *Solid State Commun.* **77** 125–8

[18] Tipcompor N, Thongtem T, Phuruangrat A and Thongtem S 2012 Characterization of SrCO3 and BaCO3 nanoparticles synthesized by cyclic microwave radiation *Mater. Lett.* **87** 153–6

[19] Baghurst D R, Chippindale A M and Mingos D M P 1988 Microwave syntheses for superconducting ceramics *Nature* **332** 311–311

[20] Feldstein H, Ben-Dor L and Beilin V 1994 Microwave synthesis of high Tc superconductors *Physica C* **235** 929–30

[21] Naitoh K, Takizawa T and Matsuse T 1999 Controlled Microwave Irradiation for the Synthesis of YBa 2 Cu 3 O 7 −x Superconductors *Jpn. J. Appl. Phys.* **38** L724

[22] Pathak L C, Mishra S K, Bhattacharya D and Chopra K L 2004 Synthesis and sintering characteristics of Y–Ba–Cu-oxide superconductors *Mater. Sci. Eng.* B **110** 119–31
[23] Edgar A D, Nicholas G R, Pedro A Q, Mark W M and Juan C N 2015 Electrospinning of superconducting YBCO nanowires *Supercond. Sci. Technol.* **28** 015006
[24] Zhang Z, Wimbush S C, Kursumovic A, Wang H, Lee J H, Suo H and MacManus-Driscoll J L 2012 Biopolymer mediated synthesis of plate-like YBCO with enhanced grain connectivity and intragranular critical current *Cryst. Eng. Comm.* **14** 5765–70
[25] Moussa M A A, Abou-Alkheer M M, El-Hefnawy S M and Al-Nattar H I A 2009 Effect of melt processing programme on microstructure and properties of YBCO thick films *J. Supercond. Nov. Magn.* **22** 687–91
[26] Zelati A, Amirabadizadeh A and Kompany A 2011 Preparation and characterization of barium carbonate nanoparticles *Int. J. Chem. Eng. Appl.* **2** 299–303
[27] Yamamoto A, Koyama T, Mito T, Wada S, Fisher R A, Phillips N E, Wang Z P and Johnston D C 2003 Magnetic properties of copper cluster-spins in $BaCuO_{2+x}$ ( $x = 0$ and 0.14), investigated by magnetization and nuclear magnetic resonance measurements *J. Phys. Condens. Matter* **15** 8587
[28] Boston R, Carrington A, Walsh D and Hall S R 2013 Synthesis of spherical superconductors *Cryst. Eng. Comm.* **15** 3763–6
[29] Chhaganlal G A, Hui-Yu C, Yu-Ming C and Grace L J 2016 Size confined magnetic phase in NiO nanoparticles *Mater. Res. Express* **3** 035017
[30] Rietveld H 1969 A profile refinement method for nuclear and magnetic structures *J. Appl. Crystallogr.* **2** 65–71
[31] Larson A C and Von Dreele R B 1987 General structure analysis system (GSAS) *Report* LA-UR-86-748 Los Alamos National Laboratory: Los Alamos, NM
[32] Gandhi A C, Chan T S and Wu S Y 2016 Structural phase transition in InSn nanoalloys and its impact on superconducting properties *J. Alloys Compd.* **688** 61–8
[33] Jain M and Gupta A 2007 3 Diamagnetic anisotropy of $BaCO_3$ *Diamagnetic Susceptibility and Anisotropy of Inorganic and Organometallic Compounds* ed R R Gupta (Berlin: Springer) pp 3033
[34] Wang Z R, Johnston D C, Miller L L and Vaknin D 1995 Static magnetization and ac susceptibility measurements of the copper-oxygen cluster compound $BaCuO_{2+x}$ *Phys. Rev.* B **52** 7384–94
[35] Zheng W-C, Mei Y, Yang Y-G and Su P 2012 Calculations of EPR g factors for the isolated tetragonal $Cu^{2+}$ (II) centre in mechanically processed $YBa_2Cu_3O_{7-\delta}$ superconductors *Phys. Scripta* **86** 025702
[36] Jones R, Janes R, Armstrong R, Pyper N C, Edwards P P, Keeble D J and Harrison M R 1990 A combined ESR/X-ray diffraction study of the Y2O3-BaO-CuO phase diagram *J. Chem. Soc. Faraday Trans.* **86** 675–82
[37] Garifullin I A, Garif'yanov N N, Alekseevskii N E and Kim S F 1991 EPR data on the evolution of the oxygen distribution in single crystals of YBa2Cu3O7−$\delta$ *Physica C* **179** 9–14
[38] Shames A I, Bandyopadhyay B, Goren S D, Shaked H and Korn C 1995 *In-situ* EPR study of room-temperature evolution of YBa2Cu3O6+x ceramics *Physica C* **252** 177–82